

NGC 741 – MERGERS AND AGN FEEDBACK ON GALAXY GROUP SCALE

G. SCHELLENBERGER,¹ J. M. VRTILEK,¹ L. DAVID,¹ E. O’SULLIVAN,¹ S. GIACINTUCCI,² M. JOHNSTON-HOLLITT,^{3,4}
S. W. DUCHESNE,^{3,4} AND S. RAYCHAUDHURY⁵

¹*Harvard-Smithsonian Center for Astrophysics, 60 Garden Street, Cambridge, MA 02138, USA*

²*Naval Research Laboratory, 4555 Overlook Avenue SW, Code 7213, Washington, DC 20375, USA*

³*School of Chemical & Physical Sciences, Victoria University of Wellington, Wellington, 6140, New Zealand*

⁴*Peripety Scientific Ltd., PO Box 11355, Manners Street, Wellington, 6142, New Zealand*

⁵*Inter-University Centre for Astronomy and Astrophysics, Post Bag 4, Ganeshkhind, Pune 411007, India*

Submitted to ApJ

ABSTRACT

Low mass galaxy cluster systems and groups play an essential role in upcoming cosmological studies such as those to be carried out with eROSITA. Though the effects of active galactic nuclei (AGNs) and merging processes are of special importance to quantify biases like selection effects or deviations from hydrostatic equilibrium, they are poorly understood on the galaxy group scale. We present an analysis of recent deep Chandra and XMM-Newton integrations of NGC 741, which provides an excellent example of a group with multiple concurrent phenomena: both an old central radio galaxy and a spectacular infalling head-tail source, strongly-bent jets, a 100 kpc radio trail, intriguing narrow X-ray filaments, and gas sloshing features. Supported principally by X-ray and radio continuum data, we address the merging history of the group, the nature of the X-ray filaments, the extent of gas stripping from NGC 742, the character of cavities in the group, and the roles of the central AGN and infalling galaxy in heating the intra-group medium.

Keywords: galaxies: groups: individual (NGC741) – X-rays: galaxies: clusters – radio continuum: galaxies – galaxies: clusters: intracluster medium – galaxies: interactions

arXiv:1707.02985v2 [astro-ph.GA] 9 Aug 2017

1. INTRODUCTION

Galaxy clusters, as the most massive gravitationally relaxed systems in the Universe, are excellent tools to study cosmology, especially the phenomena of dark matter and dark energy. The cluster mass function in particular is a sensitive probe of cosmological parameters. X-ray emission from the hot intracluster medium (ICM) traces the most massive visible component of clusters and enables derivation of both the total gravitational mass and that of the radiating baryonic component. A deep understanding of the evolution of the baryon distribution in the Universe is essential for modeling the structure formation process, especially for low-mass objects where non-gravitational effects become progressively more dominant. Furthermore, low-mass objects like galaxy groups are ideal for tracing baryons, since about 50% of galaxies reside in galaxy groups, while galaxy clusters host only a few percent (Eke et al. 1998). In the hierarchical formation process, high mass galaxy clusters are the final stage of evolution, while galaxy groups are the predominant site of merging processes. Although extended emission observed in galaxy groups can be approximated as a scaled-down version of typical cluster emission, the gas properties in groups show differences in both the scaling relations (Eckmiller et al. 2011; Lovisari et al. 2015) and AGN feedback properties (Sun et al. 2009; Bharadwaj et al. 2014); these differences contribute to the justification of the study of groups independently of clusters.

Galaxy groups show a variety of populations. The ones dominated by late type galaxies are usually poorer in hot, X-ray bright gas than the groups rich in ellipticals, and sometimes contain significant amounts of cold gas. It is well known that interactions of spiral galaxies enrich the environment (e.g., Konstantopoulos et al. 2010), leading to intergalactic HI clouds or filaments. These interactions trigger the turnover of a galaxy group being dominated by elliptical galaxies, sometimes accompanied by star formation. However, it remains unclear how the hot ICM is influenced by these processes, especially how it reaches this hot state. Although dominant sources of heat are believed to be galaxy infall and shock heating, a detailed understanding of the hot intra group medium is important for structure formation scenarios.

XMM-Newton and Chandra observations have shown in the past that feedback from the AGN in the central dominant galaxy in groups and clusters prevents the initially claimed dramatic cooling flow (e.g., Birzan et al. 2004) and is of high importance for the total energy budget for the cluster. On the other hand, the presence of star formation in these galaxies seems to indicate radiative gas cooling in the center to some extent (e.g., Allen 1995; Rafferty et al. 2008). Furthermore, major and minor mergers in the clusters and groups have a severe influence on the thermodynamic and chemical environ-

ment (e.g., ZuHone et al. 2010). While stronger mergers can create shock fronts, ram pressure stripping and cold fronts, less energetic merging events produce disturbed gas motions or displace the cores of clusters, and will also lead to a redistribution of heavy elements in the gas.

In this context, NGC 741 is a very interesting and possibly unique system: based on a relatively short X-ray exposure, it has previously been reported to host a ghost cavity, a region of low X-ray surface brightness evacuated by the central AGN. However, the non-thermal radio emission from the relativistic particles lies below the sensitivity of previous observations (Jetha et al. 2008). Furthermore, it is known to host a radio bridge between the brightest cluster galaxy (BCG) and a close member galaxy, NGC 742, as discussed in Birkinshaw & Davies (1985). Also, further extended radio emission around the BCG was detected, but, as we discuss in this work, it originates not from the AGN of the BCG, NGC 741, but from NGC 742, and marks the trajectory during the encounter of the two galaxies. The radio emission does not originate only from one double-lobed radio source, as one might at first suspect.

In this work we focus on deepening the understanding of the merger history of the NGC 741 system, including the X-ray filaments between NGC 742 and the BCG, NGC 741. For this work we make use of 150 ks of Chandra data and 80 ks of XMM-Newton data jointly awarded in Chandra cycle 16, supplemented by high resolution, multi-frequency radio images from the Very Large Array (VLA) and Giant Metrewave Radio Telescope (GMRT). Additionally, we consider the spectral properties of the system at low radio frequencies (72-231 MHz) using data from the Murchison Widefield Array (MWA).

Throughout this paper we assume a flat Λ CDM cosmology with the following parameters:

$\Omega_m = 0.27$, $\Omega_\Lambda = 0.73$, $H_0 = h \cdot 100 \text{ km s}^{-1} \text{ Mpc}^{-1}$ with $h = 0.71$, and uncertainties are stated at the 68% confidence level unless stated otherwise.

2. DATA REDUCTION AND ANALYSIS

For our analysis we employed both archival X-ray data from early in the Chandra and XMM missions — 30ks from Chandra cycle 2 and approximately 31ks from XMM-Newton — as well as deeper and more recent integrations proposed jointly in Chandra cycle 16 specifically for this work — 150ks from Chandra and 76ks from XMM-Newton (see Table 1). For the detection of spatial features and the imaging analysis we rely on the Chandra data.

For our radio study, we complement GMRT observations at 235 MHz and 610 MHz, first presented in Giacintucci et al. (2011), with an analysis of archival VLA observations at 1.4 GHz and 4.8 GHz and GMRT data at 150 MHz, taken as part of the TIFR GMRT Sky Sur-

vey (TGSS¹). We also use images and fluxes from the Galactic and Extragalactic All-sky MWA (GLEAM) survey (Wayth et al. 2015), covering the entire sky south of declination +30° with 20 frequency bands between 72 and 231 MHz, a good sensitivity of 10 mJy beam⁻¹, and an angular resolution of 100 arcsec. (In the course of the radio analysis, discrepancies noted between the GMRT 235 MHz flux density reported by Giacintucci et al. (2011) and the GLEAM extrapolation were resolved after reprocessing of the GMRT data: see §2.3.)

In the following we briefly describe our data reduction procedure.

2.1. Chandra

The three available Chandra observations (Observation ID 2223, 17198, 18718) all imaged NGC 741 on the ACIS-S3 chip and exhibit a total raw exposure time of 180 ks. We follow the standard data reduction task using the CIAO software package version 4.8 including the contributed scripts. After creating new event files using the latest CIAO calibration of March 2016 (CALDB 4.7.1) using the `chandra_repro` task, we perform a lightcurve cleaning to detect flares in the data. We did not detect any bad time intervals, so the final exposure times are 30 ks, 91 ks and 59 ks, respectively for observation ID 2223, 17198 and 18718. For the spectral analysis we use the `xspec` software version 12.9.0o included in Heasoft 6.18. This includes the updates² to `xspec` to correct for the underestimation of `apec` normalization and abundance by a factor of $1 + z$. The spectral background was taken into account by using the provided blank sky observations, with a normalization factor scaled by the count rate at high energies, (9.5 – 12) keV. For outer low surface brightness regions we use the stowed events files (recording the particle background) and simultaneously fit the RASS spectra to them³.

2.2. XMM-Newton

To reduce the XMM-Newton EPIC observation (0748190101) we used the default tasks `emchain` and `epchain` within the SAS software package (version 15.0.0). The observation was split into two parts of 3.5 ks and 71 ks exposure time in the MOS data, but for the following procedure we ignored the short part. For MOS data we included all events with `PATTERN <= 12` and flagged `#XMMEA_EM`, while for PN data we included only `PATTERN <= 4` and `FLAG==0`. The PN data were corrected for out-of-time events. The lightcurve cleaning was performed using the ESAS tasks `mos-filter`

¹ <http://tgssadr.strw.leidenuniv.nl>

² <https://heasarc.gsfc.nasa.gov/docs/xanadu/xspec/issues/issues.html>

³ <http://heasarc.gsfc.nasa.gov/cgi-bin/Tools/xraybg/xraybg.pl>

Table 1. X-ray and optical data for NGC 741

Instrument	Observation	exposure	resolution
Chandra/ACIS-S	2223	30 ks	0.5''
Chandra/ACIS-S	17198	91 ks	0.5''
Chandra/ACIS-S	18718	59 ks	0.5''
XMM/EPIC	0748190101	30 ks	10''
HST PC	6587	4.2 ks	0.05''

NOTE—Column 3 refers to the X-ray exposure time remaining after lightcurve cleaning (only the XMM exposure time was significantly reduced).

and `pn-filter`, resulting in a 60% reduction in useful exposure time. The spectral background was modeled following the procedure described in Mernier et al. (2015).

2.3. GMRT data

We reduced an archival TGSS pointing at 150 MHz (R07D37) observed at 2h0m0s +05d48m00s and containing NGC 741, and re-processed the 235 MHz and 610 MHz observations from Giacintucci et al. (2011). Details are summarized in Table 2. The data were calibrated and reduced using the NRAO⁴ Astronomical Image Processing System (AIPS). All data were collected in spectral-line observing mode using the *GMRT* hardware backend. Data affected by radio frequency interference (RFI) were excised using RFLAG, followed by manual flagging to remove residual bad data. Gain and band-pass calibrations were applied using the primary calibrators 3C286 and 3C147 at 150 MHz and 3C48 and 3C147 at 235 MHz and 610 MHz. The Scaife & Heald (2012) scale was used to set their flux densities at 150 MHz and 235 MHz; the VLA 1999.2 coefficients in SETJY were used at 610 MHz. Phase calibrators, observed several times during each observation, were used to calibrate the data in phase. A number of phase self-calibration cycles, followed by a final self-calibration step in amplitude, were applied to the target visibilities. Non-coplanar effects were taken into account using wide-field imaging at all frequencies, decomposing the primary beam area into smaller facets. We note that the flux discrepancy between the 235 MHz flux in Giacintucci et al. (2011) and the GLEAM extrapolation was found to be the result of errors driven by one GMRT antenna (C12) located in the compact core. Removal of this antenna brought the fluxes into better agreement.

⁴ National Radio Astronomy Observatory.

Table 2. Summary of the radio observations

Array	Project	Frequency (GHz)	Bandwidth (MHz)	Date	Time (min)	FWHM (" × ")	r.m.s (mJy beam ⁻¹)
GMRT	19_043 ^a (R07D37)	0.15	16	2010 Oct 30	15	25 × 25	6.5
GMRT	12SGA01	0.24	8	2007 Aug 31	140	14 × 9	0.3
GMRT	10SGA01	0.61	32	2006 Aug 27	140	7 × 4	0.05
VLA – DnC	AH276	1.4	12.5	1988 May 19	112	23 × 16	0.06
VLA – D	AB593	4.8	12.5	1991 May 24	43	23 × 16	0.05
VLA – BnA	AB593	4.8	12.5	1991 Dec 16	39	2 × 1	0.03

NOTE—Column 1: Radio telescope. Column 2: project code. Columns 3–6: observing frequency, bandwidth, date and total time. Column 7: full-width half maximum (FWHM) of the array (obtained for ROBUST=0 in IMAGR). Column 8: image r.m.s. level (1σ).

Table 2 summarizes restoring beams and root mean square (r.m.s) noise levels (1σ) of our final GMRT images, obtained setting the Briggs robust weighting (ROBUST) to 0 in IMAGR (Briggs 1995). Finally, we corrected the images for the GMRT primary beam response⁵ using PBCOR. Residual amplitude errors are estimated to be within 15% at 150 MHz and 10% at 327 MHz and 610 MHz.

2.4. VLA data

We reduced VLA continuum-mode observations of NGC 741 at 1.4 GHz and 4.8 GHz obtained from the VLA archive (Table 2). The data were calibrated and reduced in AIPS. The flux density scale was set using the VLA 1999.2 coefficients for 3C286 and 3C48 in SETJY. Several loops of imaging and self-calibration were applied to reduce the effects of residual phase and amplitude errors in the data. All images were made using ROBUST=0. Correction for the VLA primary beam attenuation was applied to the images using PBCOR. Residual amplitude errors are within 5% at all frequencies.

2.5. MWA data

We use the source-finding software DUCHAMP (Whiting 2012) to measure the flux density in the MWA sub-band images. For these measurements, we use a growth threshold of $2\sigma_{\text{rms}}$ which allows integration of the flux density out to that $2\sigma_{\text{rms}}$ value after detection of the source. The local noise in the image is determined by

use of the Background And Noise Estimation tool, BANE⁶, which performs background calculation and the deviation from this background. Rather than calculating this using every pixel at once, BANE uses sparse pixel grids not only to save computational time, but also to account for cases where the noise changes significantly over the image. Uncertainties in integrated flux densities are not left to DUCHAMP as we do not use the built-in noise calculation tool. Uncertainties are derived from

$$\sigma_{S_\nu} = \sqrt{(fS_\nu)^2 + \left(\sigma_{\text{rms}}\sqrt{N_{\text{beam}}}\right)^2} \quad [\text{Jy}], \quad (1)$$

where N_{beam} is the the number of beams crossing the source, and f is the additional percentage uncertainty associated with the flux density scale of the image. In the case of the MWA GLEAM images, this is 8 per cent at the declination of NGC 741.

3. RESULTS

Our main results on the group properties and its dynamical state are summarized in this section, where we look at the different wavelength regimes separately. The X-ray emission is determined by the thermodynamical properties of the ICM, while radio observations are sensitive to the non-thermal processes in galaxy clusters, such as particle acceleration in shocks or AGNs.

3.1. X-ray picture

The X-ray data allow us to characterize the galaxy group NGC 741 as a whole. The spectral and surface brightness analysis follows the descriptions outlined in

⁵ <http://www.ncra.tifr.res.in:8081/~ngk/primarybeam/beam.html>

⁶ <https://github.com/PaulHancock/Aegean/wiki/BANE>

Schellenberger & Reiprich (2017). For this analysis the center of the group is chosen to be the emission peak of an 25 arcsec Gaussian-smoothed, exposure corrected image, because an emission weighted approach would shift the center clearly toward NGC 742 due to the extended emission. Using the emission peak (RA 1:56:21, Dec +5:37:45) the center coincides with the galaxy NGC 741, which we assume to be in the center of the mass halo, and NGC 742 is just a lower mass intruder. For all further analyses the redshift is frozen to 0.0185 (Huchra et al. 1999) and the hydrogen column density to $5.11 \times 10^{20} \text{ cm}^{-2}$ (Willingale et al. 2013).

We investigate the morphology, perform a spectral analysis of the thermal emission of the hot ICM, and, by assuming hydrostatic equilibrium, calculate the total gravitating mass. The knowledge of general system properties, such as temperature and mass, is crucial to interpret irregular phenomena (e.g., mergers, shocks).

3.1.1. General X-ray morphology

Figure 1 shows XMM-Newton and Chandra X-ray images superposed radio contours. The radio emission arises from non-thermal synchrotron processes which lead to a power-law spectrum (at first approximation). In this case it is the superposition of two sources, the AGN emission of NGC 741 and NGC 742, which leads to the given spatial distribution. On very small scales, it is even possible to trace the emission from the bent radio jets of NGC 742. The left panel shows the XMM-Newton data overlaid with GMRT radio contours at 235 MHz. In the core we see NGC 741 and NGC 742 within the irregularly shaped X-ray emission of the galaxy group, while at larger distances, three other galaxies can be identified (see Section 3.1.4). The right panel shows the Chandra data, zoomed-in on the core region, overlaid with the VLA-BnA 5 GHz contours of the radio emission between the two galaxies in the core (see also Fig. 6). Furthermore, we are able to identify several filaments in the X-rays: The X-ray filament connection NGC 741 and NGC 742, a north-east filament or sub-clump and also two line-shaped features to the south of the core (see also Fig. 2). To the west of NGC 741 we notice a decrease in the X-ray surface brightness, which might be a hint of a cavity or recent merging activity. Although the galaxy group appears to be dynamically disturbed, there exists a very peaked surface brightness in the core indicating the presence of a cool core.

We extract the radial surface brightness profile of the Chandra data in the (0.5 – 2.0) keV band and correct for vignetting and variations in the exposure time using the `merge_obs` task (see Fig. 3 left bottom). We find a steeper surface brightness profile to the south-west when we fit several sectors separately. The excess emission to the north-east is related to an extended source, which seems to be related to the galaxy group. As already indicated in Fig. 1 (right) there are at least two small X-ray filaments to the south (west) of NGC 741. We

analyze those in more detail in Fig. 2. The cylindrical shape of these objects seems remarkable, and they are almost perpendicular to each other. The one aligned to the south-west lies at the edge of the south-west radio tail.

Other bright features in the residuals image are the X-ray filament between NGC 741 and NGC 742 (0.15×0.86 arcmin in size), and a $\sim 15\sigma$ decrease in surface brightness to the west of NGC 741 (see discussion on the cavity in Sec. 4.2).

3.1.2. Spectral analysis

For spectral extraction we use the `specextract` task provided with the CIAO software package. Since we are dealing with regions of few photon counts, we use the C statistic (Cash 1979) during the spectral fitting and apply a minimum number of 1 count per spectral bin. To account for the co-variance between fitting parameters (e.g., temperature and abundance) we use the Metropolis MCMC algorithm implemented in `xspec`, and calculate derived quantities (like the entropy) from the chains.

The spectral modeling of the ICM emission is described by an absorbed thermal model (`phabs×apec`) using the AtomDB code version 2.0.2 (Foster et al. 2012). The relative abundance of heavy elements is set to the values of Asplund et al. (2009).

Figure 3 shows the projected temperature profile extracted in annuli centered on the NGC 741 X-ray peak and excluding point sources detected by the `wavdetect` task. The galaxy group exhibits a cool core with a temperature below 1 keV in the center, and a peak temperature of around 2 keV, which is unusually high for a system of this size. At larger radii the temperature drops to about (1.3 – 1.4) keV. The XMM-based profile of the relative abundance of heavy elements (Fig. 3) shows a sharp increase in the central bin, but this might be related to the larger PSF, since the distribution of heavy elements is complicated in this object.

We compute a hydrostatic mass at a radius where the density within that radius has dropped to 500 times the critical density of the Universe ($R_{500} = 560 \pm 15 \text{ kpc} = 25.2 \pm 0.7 \text{ arcmin}$) of $M_{500} = 5.2 \pm 0.4 \times 10^{13} M_{\odot}$. The mass profile was extrapolated using an NFW model with the $c - M$ relation from Bhattacharya et al. (2013). More details on this procedure are given in Schellenberger & Reiprich (2017). The gas mass at this radius is $M_{\text{gas},2500} = 8.6 \pm 0.3 \times 10^{11} M_{\odot}$, which leads to a gas mass fraction of $f_{\text{gas},2500} = 2.9 \pm 0.1 \%$. This value is at the lower end of what is expected for galaxy groups (Sun et al. 2009; Lovisari et al. 2015).

The entropy of the galaxy cluster ICM can be derived from the temperature and gas density,

$$K = kT \cdot n^{-\frac{2}{3}} . \quad (2)$$

This quantity is essential to study non-gravitational effects within the ICM (see, e.g., Ponman et al. 1999;

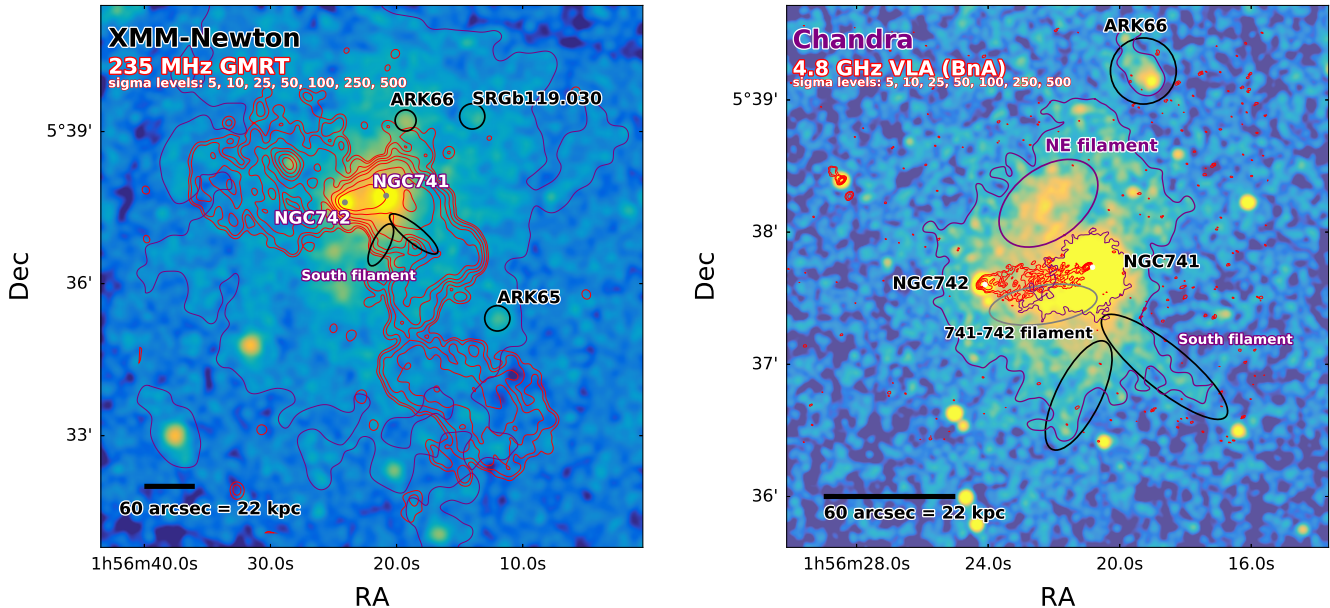


Figure 1. Smoothed and exposure corrected image from the combined XMM-Newton/EPIC (left) and from the Chandra ACIS (right) detectors. Red contours show the radio emission detected with the GMRT at 235 MHz (left) and with the VLA at 4.8 GHz (right), and the purple and white contours follow the smoothed X-ray surface brightness. Angular resolution and 1σ noise values of the radio images are as listed in Table 2.

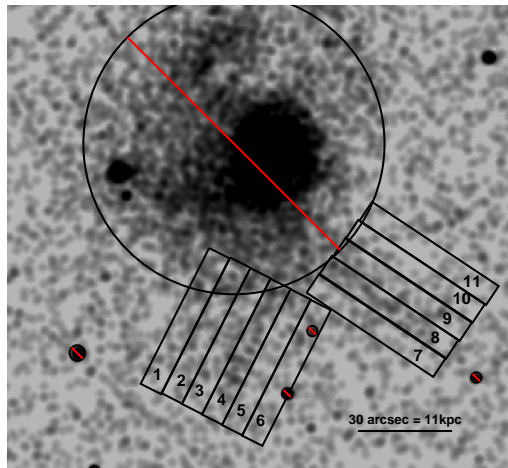
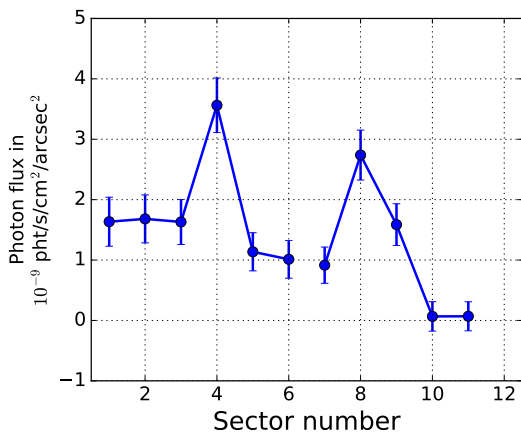


Figure 2. Chandra surface brightness distribution in the region south to the core where two line-shaped filaments can be identified.

Cavagnolo et al. 2009). We constrain the central entropy of the core to 12 ± 1 keV cm², which is typical for cool core systems. In a region immediately around the AGN of NGC 742 we find 7.8 ± 1.3 keV cm². In an annular region (from 6 kpc to 12 kpc) we find an entropy 39 ± 2 keV cm²; although the X-ray filament connecting the AGN of NGC 741 and NGC 742 lies mainly in the same region as this annulus, we find an entropy of 9.9 ± 0.6 keV cm⁻² in the filament, assuming it has a cylindrical shape. The pressures of the gas in the fila-

ment and in the annulus are in rough equilibrium, although there is a hint that the pressure in the X-ray filamentary gas is slightly higher. We analyzed regions in the XMM-Newton data along the south-west radio tail (see Fig. 1 left panel, and Section 3.2.3) to find hints for the origin of the gas. The available data do not give any conclusions for a different entropy in the regions of the south-west radio tail.

3.1.3. Temperature and metallicity maps

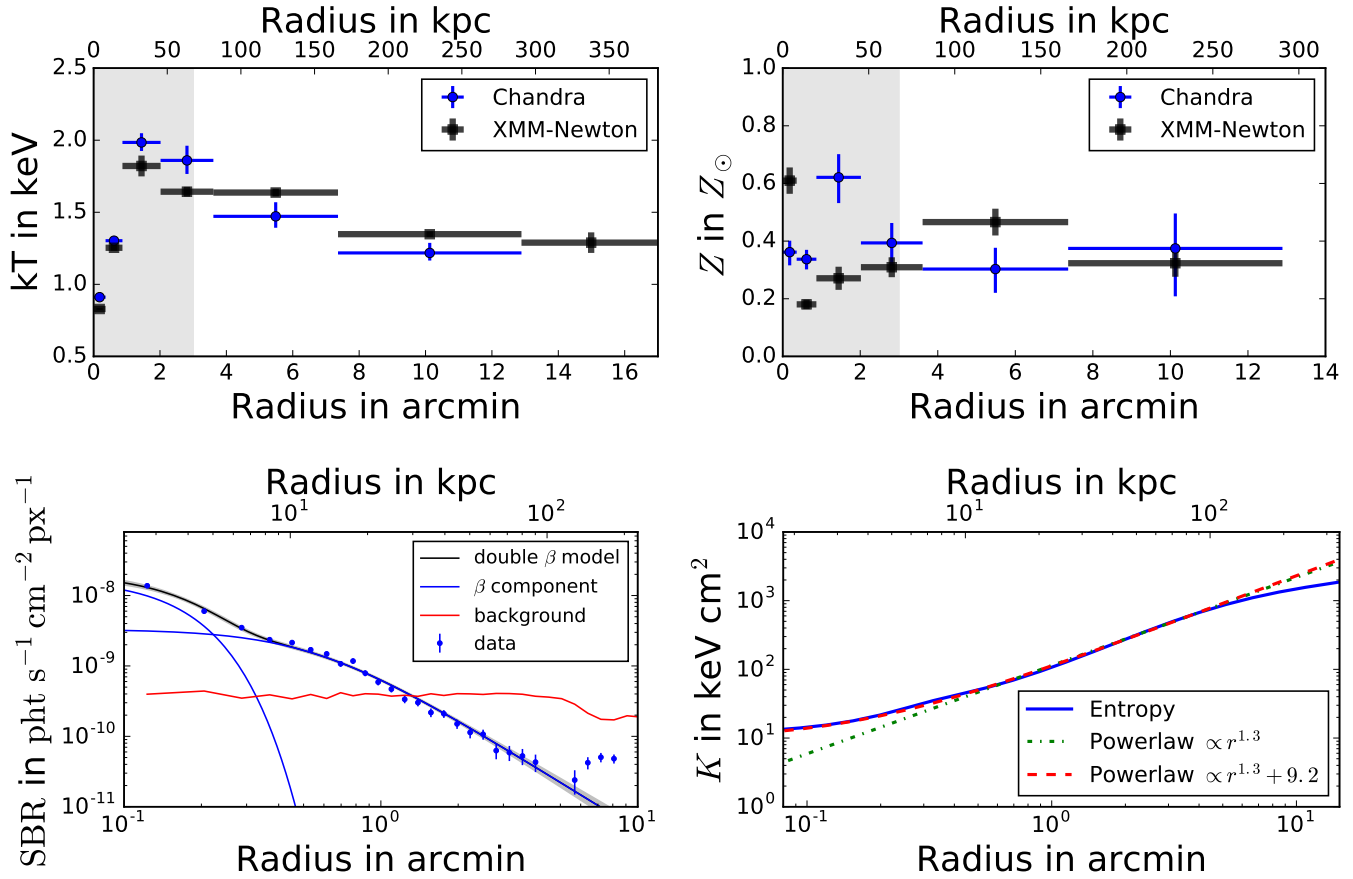


Figure 3. *Top:* Projected temperature (left) and abundance (right) profiles of the Chandra and XMM-Newton data. The gray area indicates where the Chandra FOV covers the all parts of the cluster, otherwise the extraction is along the Chandra S-chips array in NW-SE direction. *Bottom:* Surface brightness (SBR, left) and entropy (right) profiles.

We construct gas temperature and metallicity maps by dividing the images into three different energy bands. Appendix A explains the details of this method. While the absolute values of temperature and metallicity might be slightly biased with this method, we are mainly interested in identifying local variations in the gas temperature and metallicity on small spatial scales. Figure 4 shows the resulting maps for NGC 741. The images are initially adaptively binned (using the CIAO task `dmnautilus`) to achieve a signal-to-noise of 15 in the Fe-L line (0.7-1.3 keV) and then Gaussian smoothed with $\sigma = 1.5$ arcsec. We do not consider any regions where the source count rate in the broad energy band is less than 33% of the background count rate.

For the large-scale temperature distribution, we find a similar trend as derived from our full spectroscopic analysis; however, it seems that there is an elongation of cooler gas along the north-south direction. There is also a sudden 50% increase in the temperature east of NGC 742. The connection between NGC 741 and NGC 742 is filled mostly with cooler gas, but there is also some slightly warmer gas, indicating that the gas between the two galaxies has had enough time to mix

with the surrounding, slightly hotter ICM. To the north-east of NGC 741 we detect another cooler region that corresponds to an enhanced surface brightness region. Finally, there is cooler gas to the south-west of NGC 741 that corresponds to the filament seen in Fig. 2 (region 8).

The abundance map shows, on average, a low metallicity of about 0.1 to 0.3 solar. These abundances are lower than those shown in the azimuthally-averaged abundance profile, but the abundance map shows that there are local peaks and enhancements in the metallicity. Most of the higher abundance regions are located toward the south of NGC 741. Indeed, we verified with a full spectroscopic analysis that these spatial fluctuations in the metallicity are real. For this analysis we used the C-statistic and an MCMC approach. Contrary to the spectroscopic analysis, we find a high abundance of heavy elements in the center of NGC 741.

3.1.4. Other galaxies and AGNs

In the normalized residuals image of the surface brightness, we identify three smaller X-ray halos related to group member galaxies (see Fig 1). Two of them

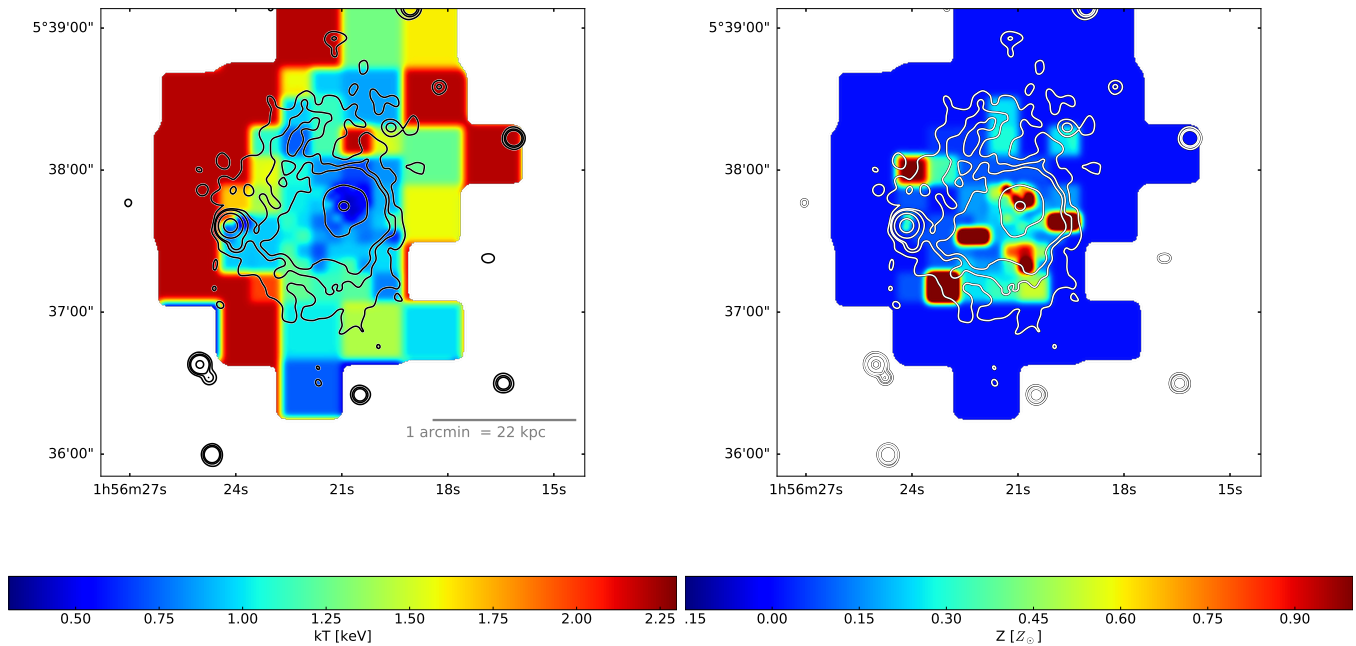


Figure 4. Temperature and metallicity maps for NGC 741 with the soft X-ray band contours overlaid. Only regions with a source-to-background ratio of at least 1.33 are shown. See text and Appendix A for details.

have been mentioned before by Jeltema et al. (2008), ARK66 and ARK65, while SRGb119.030 has not previously been identified in the X-rays. Only ARK66 is bright enough for a spectroscopic analysis and we measure a temperature of $0.33^{+0.09}_{-0.04}$ keV and a luminosity of $L_{X,0.5-2.0} = 9.4^{+1.9}_{-1.4} \times 10^{39}$ erg s $^{-1}$. For the other two galaxies, we are able to constraint only the luminosity with a reasonable precision. For SRGb119.030 we obtain $L_{X,0.5-2.0} = 2.6^{+0.7}_{-0.4} \times 10^{39}$ erg s $^{-1}$, and for ARK65 we obtain $L_{X,0.5-2.0} = 3.2^{+0.4}_{-0.4} \times 10^{39}$ erg s $^{-1}$. Based on the K-band luminosities, ARK66 has an unusually high X-ray luminosity. In the case of ARK66, the X-ray emission has a head-tail structure, suggesting that the galaxy is moving toward the south-west. This head-tail structure is likely to be gas that has been ram-pressure stripped from the galaxy (also see recently discovered X-ray tails associated with other galaxies, e.g., Sun et al. 2006; Schellenberger & Reiprich 2015). From measured redshifts by Mahdavi & Geller (2004); Lavaux & Hudson (2011), we find a line-of-sight velocity difference between ARK66 and NGC 741 of 772 ± 9 km s $^{-1}$. Since we see an extended tail behind ARK66, the trajectory of ARK66 cannot be exactly along the line-of-sight. If we assume a 45° orbital inclination relative to the plane of the sky, then the 3D velocity must be about 1100 km s $^{-1}$, which is relatively high given the projected distance from the group center of 32 kpc.

A comparison of the X-ray fluxes for the AGN in the centers of each galaxy (NGC 741 and NGC 742), shows that there is no significant variation over almost 15 years for NGC 741, but there is a 50% flux increase for the

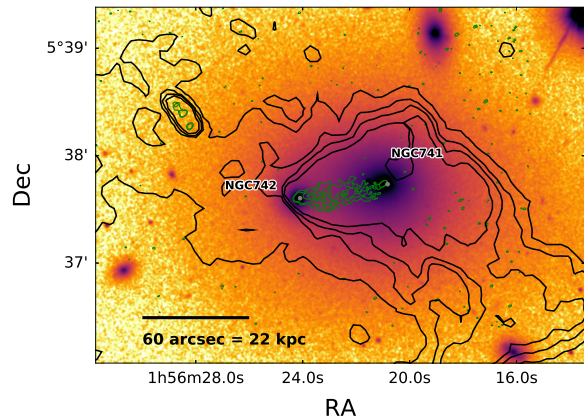


Figure 5. SDSS r-band image with radio contours overlaid: In black 610 MHz GMRT contours (5, 25, 50, 100 σ), and VLA 5 GHz contours in green (5, 13 σ).

AGN in NGC 742. The current flux of the AGN in NGC 742 is $1.30 \pm 0.04 \times 10^{-13}$ erg s $^{-1}$ cm $^{-2}$, while the flux of the AGN in NGC 741 is about two orders of magnitude lower.

3.2. Radio picture

The radio emission traces the synchrotron emission of high energy particles that were ejected by the AGN. By analyzing the radio fluxes in different bands, we can draw conclusions on the emitted energy, age of the particles, and magnetic field strength. We have data available from the GMRT, VLA and the MWA on NGC 741.

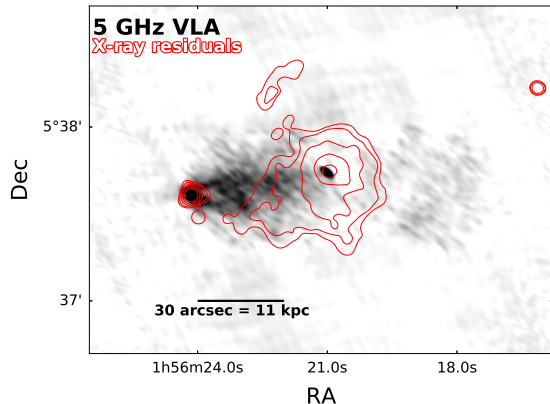


Figure 6. Radio jets of NGC742, formerly classified as bridge connecting NGC 742 and NGC 741.

We initially identify extended emission and point sources at all frequencies. The broad, extended emission can be seen in Fig. 1 with the X-ray emission and Fig. 5 on top of the optical SDSS data. The radio emission to the east of NGC 741 extends approximately 80 kpc from the central AGN, while the radio tail to the south-west has a maximum extent of 110 kpc.

3.2.1. The bent jets of NGC742

The high resolution image at 5 GHz with a beamsize of 2×1 arcsec (see Fig. 6), provides a more detailed view of the radio emission between NGC 742 and NGC 741. NGC 742 appears to be a head-tail radio galaxy with strongly bent jets to the west. The emission is brightest around NGC 742 and becomes fainter toward the west. We also see the v-shaped structure of the jet around NGC 742, typical for bent radio jets. The radio surface brightness decreases toward NGC 741, beyond which we do not detect small scale radio emission. NGC 741 itself does not show any radio jets and is only visible as a point source. From a high resolution VLA observation at 1.4 GHz, we detect a clear spectral steepening from NGC 742 to NGC 741, with spectral indices⁷ between -0.5 and -1 (M. Birkinshaw, private communication). In Section 4.3 we present a discussion concerning the shape of the bent jets.

3.2.2. Radio spectrum

To compare the radio emission of NGC 741 with other telescopes, we need to compute the integrated flux.

⁷ we define the spectral index α as $S_\nu \propto \nu^\alpha$, where S_ν is the flux density at frequency ν

Table 3. Radio fluxes for NGC 741

Instrument	Frequency	Flux
	MHz	Jy
VLSS-R	74	10.36 ± 0.79
MWA/GLEAM	76	8.58 ± 0.72
MWA/GLEAM	84	7.45 ± 0.62
MWA/GLEAM	92	6.78 ± 0.57
MWA/GLEAM	99	6.22 ± 0.52
MWA/GLEAM	107	6.25 ± 0.52
MWA/GLEAM	115	6.13 ± 0.50
MWA/GLEAM	122	5.54 ± 0.45
MWA/GLEAM	130	5.37 ± 0.44
MWA/GLEAM	143	5.21 ± 0.43
MWA/GLEAM	150	4.89 ± 0.40
MWA/GLEAM	158	4.67 ± 0.38
MWA/GLEAM	166	4.51 ± 0.37
MWA/GLEAM	173	4.34 ± 0.36
MWA/GLEAM	181	4.09 ± 0.34
MWA/GLEAM	189	4.04 ± 0.33
MWA/GLEAM	196	3.76 ± 0.31
MWA/GLEAM	204	3.68 ± 0.31
MWA/GLEAM	212	3.57 ± 0.30
MWA/GLEAM	220	3.47 ± 0.29
MWA/GLEAM	227	3.53 ± 0.30
GMRT	150	5.44 ± 0.82
GMRT	240	4.25 ± 0.43
GMRT	613	1.61 ± 0.16
NVSS	1400	1.04 ± 0.05
VLA (DnC)	1411	1.02 ± 0.05
VLA (DnC)	4841	0.30 ± 0.02
Becker+ 1991	4850	0.31 ± 0.03

We calculate integrated fluxes and uncertainties in our high resolution images from VLA and GMRT using the `radioflux` python tool by M. Hardcastle⁸. In addition, data from the MWA GLEAM survey was measured using the Duchamp software package (Whiting 2012).

The flux densities are summarized in Table 3 along with the fluxes from GLEAM, VLA Low-Frequency Sky Survey Redux (VLSS-R) at 74 MHz (Lane et al. 2014), NVSS survey at 1.4 GHz (Condon et al. 1998), and the 4.85 GHz flux reported by Becker et al. (1991). We note that our GMRT flux at 150 MHz (5.44 ± 0.82 Jy) is significantly higher than the flux of 2.58 ± 0.26 Jy reported in the catalog from the TGSS Alternative Data Release

⁸ www.extragalactic.info/~mjh/radio-flux.html

(Intema et al. 2017). By integrating the flux directly on the TGSS-ADR mosaic image, we find a slightly higher value of 3.58 ± 0.54 Jy, which, however, is still in disagreement with our flux at $\sim 1.9\sigma$ level and MWA flux ($\sim 2\sigma$) at 150 MHz. The integrated radio spectrum is shown in Fig. 7.

The data are given on the Scaife & Heald (2012) flux density scale, while the MWA data are given on the Baars et al. (1977) flux density scale. As there are no calibrated flux density scales well suited for frequencies below 240 MHz (Perley & Butler 2017), we expect only a small difference between these scales ($\leq 2\%$). We do not attempt to correct to a single flux scale. Nevertheless, we note that the GMRT spectrum shows broad agreement with a single power-law model with an overall slope of 0.76 ± 0.01 between 74 MHz and 5 GHz.

3.2.3. Spectral study of the south-west tail

For a detailed analysis of the south-west radio tail using the GMRT and VLA imaging data (150 MHz to 4.8 GHz), we homogenized all images which have different resolutions and UV-coverage using the CASA software. All images have been produced using the same uv-range, Gaussian-smoothed to 25 arcsec (the beam of the lowest resolution image), and re-gridded. In Fig. 8 and Fig. 9 we show all regions where a spectral index could be computed (i.e., regions where the flux exceeds twice the noise level at all frequencies). The circle and triangle mark the positions of NGC 742 and NGC 741, respectively. The other points give the spectral index and synchrotron age of different interesting regions. The spectral age is computed from the break frequency obtained by fitting a power-law spectrum with an exponential cut-off as in the JP model (Jaffe-Perola, see e.g., Carilli et al. 1991). Following Slee et al. (2001), the age is then calculated from:

$$\frac{t_{\text{age}}}{\text{Gyr}} = 1.59 \frac{\sqrt{B}}{B^2 + B_{\text{CMB}}^2} \left((1+z) \frac{\nu_{\text{break}}}{1 \text{ GHz}} \right)^{-\frac{1}{2}}, \quad (3)$$

where the magnetic field B is given in μG and the inverse Compton losses are accounted for with the equivalent magnetic field of the CMB, $B_{\text{CMB}} = 3.25(1+z)^2 \mu\text{G}$. We assume $B = 2 \mu\text{G}$, but the dependence of the age on the magnetic field strength is weak ($1 \mu\text{G}$ decreases the age by 5%, while $5 \mu\text{G}$ decreases the age by 28% with respect to our default choice). To better constrain the spectral age we assume that the power-law component has a fixed slope of -0.76 , which agrees with the radio spectrum of the integrated source.

The flattest spectrum is located around NGC 742, as also indicated by the high resolution images in the previous section. We also detect that along the south-west radio tail, the spectral index shows a clear steepening (up to an index of -1.2 to -1.3). The general shape of the south-west tail cannot be easily explained, for example by gravitational bending or galactic motion, but

was probably caused by gas sloshing in the ICM which perturbed the end of the tail (and also the older particle population) to the south. Similar shapes have also been seen in other head-tail radio galaxies (e.g., for 3C 465 see Eilek et al. 1984) and the bent radio jet in NGC5044 by David et al. 2009.

3.3. Optical

We use the available HST data at 555 nm, taken with the Wide-Field Planetary Camera 2 (WFPC2) from the Hubble Legacy Archive (HST Proposal 6587), to fit 2D Sersic models to the two galaxies NGC 741 and NGC 742 with the addition of a constant background (using *sherpa*). Both galaxies have a Sersic index of about 1 (1.2 and 1.6) as expected for giant elliptical galaxies. Subtracting these 2D Sersic models from the HST image shows there are no significant surface brightness residuals near NGC 741, but there are clear residuals in the form of rings around the center of NGC 742 (see Fig. 10). The 2D Sersic model allows for ellipticity, but the eccentricity is only 1% and consistent with 0. The red ring in Fig. 10 may be due to the recent encounter with NGC 741 or the recent accretion of a gas rich dwarf galaxy. The formation of rings after a close encounter has been seen in literature, even for early type galaxies (Nair & Abraham 2010; Mapelli & Mayer 2012; George 2017).

4. DISCUSSION

4.1. Gas cooling

To investigate the importance of gas cooling and thermal instabilities in the group center, we computed the ratio of the cooling time to the free-fall time, $\frac{t_{\text{cool}}}{t_{\text{ff}}}$, as suggested, e.g., by Voit et al. (2015) or Hogan et al. (2017). At a distance of 18 kpc from the group center (approximately the distance to NGC 742), the ratio is about 100, while in the center of the group near 1 kpc, the ratio drops to approximately 10 (see the values in Tab. 4). This corresponds to the threshold where the growth of thermal instabilities due to cooling becomes significant. Several other basic ICM parameters are also summarized in Tab. 4. We conclude for our group that the amount of cold gas within the region of the BCG and its supermassive black hole is not refilled fast enough to allow star formation (SF) to be initiated. There is no available $H\alpha$ data, but we can estimate the SF rate from the WISE data (using W3 and W4 bands as in Lee et al. 2013; Jarrett et al. 2013). Compared to studies like, e.g., McDonald et al. (2016), we get a fairly low SF rate for NGC 741 of about $0.25 M_{\odot} \text{ yr}^{-1}$.

The entropy profile derived from the deprojected temperature profile has a relatively steep slope of 1.35 ± 0.02 , an entropy of $796 \pm 5 \text{ keV cm}^2$ at 100 kpc, and an extrapolated central entropy of $9 \pm 2 \text{ keV cm}^2$. In general, galaxy groups show a larger scatter in the slope of the entropy profile compared to rich clusters

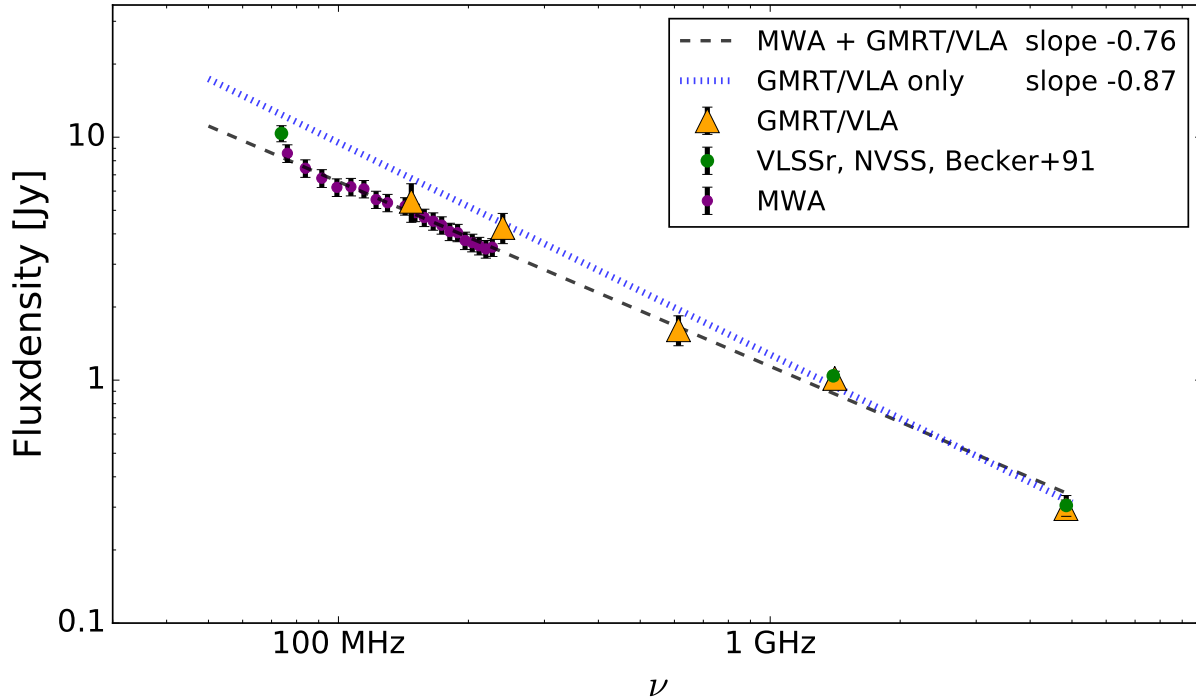


Figure 7. Integrated radio spectrum of NGC 741.

Table 4. Gas properties at small radii round the galaxy NGC 741.

R [kpc]	t_{cool} [Gyr]	$t_{\text{cool}}/t_{\text{ff}}$	n_e [cm^{-3}]	K [keV cm^2]	\dot{M}_{classic} [$\frac{M_{\odot}}{\text{yr}}$]
(1)	(2)	(3)	(4)	(5)	(6)
1	0.45 ± 0.04	12 ± 5	$(9.2 \pm 0.5) \times 10^{-3}$	12 ± 1	$(2.4 \pm 0.3) \times 10^{-3}$
10	3.05 ± 0.16	50 ± 6	$(2.5 \pm 0.1) \times 10^{-3}$	45 ± 2	$(8.1 \pm 0.6) \times 10^{-2}$
50	60 ± 5	483 ± 36	$(3.6 \pm 0.2) \times 10^{-4}$	317 ± 16	$(1.6 \pm 0.2) \times 10^{-1}$

(1) Distance from core of NGC 741. (2) Cooling time at R . (3) Ratio of the cooling and free-fall time indicating thermal instabilities. (4) Electron number density from model. (5) Entropy. (6) Classical mass deposition rate.

(Sun et al. 2003; Cavagnolo et al. 2009). Since the slope of the entropy profile is steeper than that expected from purely gravitational heating (slope of 1.1; Tozzi & Norman 2001), the outer regions of the group must have been strongly affected by the central AGN. Examining the gas mass fraction as a function of radius, we find a slight decrease in the region between 20 and 100 kpc. Together with the steep entropy profile, we conclude that, at intermediate scales, the galaxy group is relatively gas poor and cannot cool efficiently. In addition, the cooling time near 50 kpc is about five times the Hubble time, much more than expected for a group (e.g.,

Sanderson et al. 2006). This is the likely reason for the temperature peak between 1 and 2 arcmin.

4.2. Cavities

4.2.1. Jetha+08 cavity

In our deep X-ray observations we do not clearly detect the previously claimed X-ray cavity to the west of NGC 741 (Jetha et al. 2008), marked in Fig. 11. We estimate the decrease in number of counts assuming the cavity region (modeled as a sphere for simplicity) is completely depleted of thermal gas. Assuming our double-beta parametrization of the surface brightness profile, we estimate 731 counts from the ICM along the line of

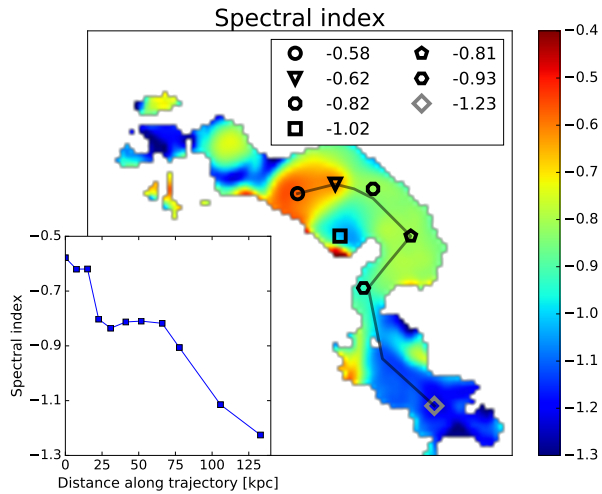


Figure 8. Radio spectral index map using the GMRT and VLA data from 150 MHz to 4.8 GHz (see Section 3.2.2). The markers show regions of interest and the legend lists the spectral index at that point. The lower left panel shows the spectral index along the assumed trajectory of NGC 742.

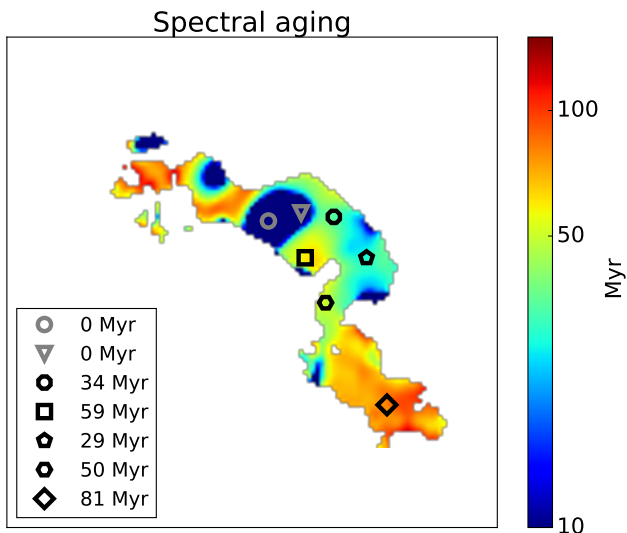


Figure 9. Spectral aging map derived from the calculation of the break frequency (Eq. 3) assuming a power-law slope of -0.76 .

sight to the cavity, of which 105 counts originate from within the cavity volume. Including about 530 background counts in the calculation (total 1261 ± 36 cts), a completely empty cavity would be significant at a 3σ level. The fact that we measure exactly 1254 cts within the cavity indicates that there is no surface brightness decrease, assuming our model is correct.

Nevertheless, we calculate the enthalpy of the claimed cavity from the density and temperature profiles using

$$H = \frac{\gamma}{\gamma - 1} pV, \quad (4)$$

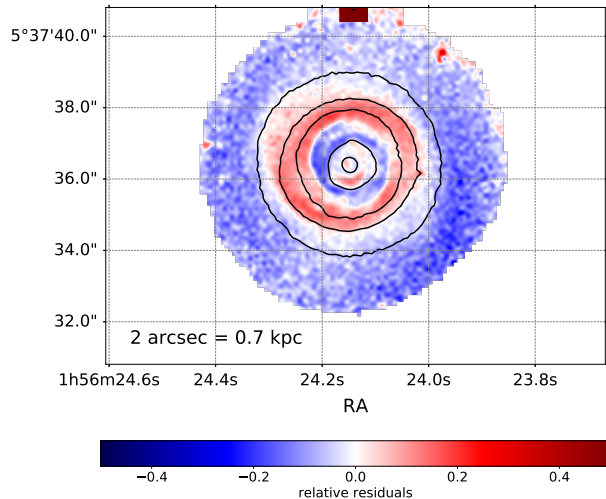


Figure 10. NGC 742 Residuals of the HST image 555 nm after subtracting the best-fit 2D Sersic model. Red (blue) regions have a higher (lower) flux than the model prediction. Contour lines follow the optical surface brightness.

where $\gamma = \frac{4}{3}$ for a fully relativistic gas, and p is the pressure within the volume V . We find a value of $2.1 \pm 0.2 \times 10^{58}$ erg. In order to determine the nature of the any existing cavity, we compare, as in Panagoulia et al. (2014b), the cooling luminosity, inferred within a region where the cooling time is shorter than 3 Gyr (see Panagoulia et al. 2014a), in our case 10 kpc, with the enthalpy divided by the sound crossing time t_s . The spectral analysis gives us a cooling luminosity of $2.59 \pm 0.04 \times 10^{41}$ erg s $^{-1}$. With the sonic timescale, $t_s = 27$ Myr, we estimate cavity power to be 2.6×10^{43} erg s $^{-1}$, which is two orders of magnitude above the measured luminosity. We conclude that the claimed cavity is too large and too close to the core of the BCG. It cannot be a young structure still being powered by the AGN jets. We therefore cannot confirm the existence of the ghost cavity, and it seems likely that it was misidentified owing to the asymmetry of the surface brightness distribution.

4.2.2. Small west cavity

We find in the normalized residual image (Fig. 11) a strong decrease in surface brightness (25σ with respect to the surrounding annulus) about 16 kpc west of NGC 741. This seems to be a very good candidate for a cavity inflated by the NGC 741 AGN, especially because the radio emission seems to roughly overlay the feature seen in the X-rays. Within the circular region (8 kpc radius) of the cavity we measure 397 cts, while we would expect 702 cts from the surface brightness and density profiles. A completely empty sphere at this position would reduce the number of counts only by 69 cts,

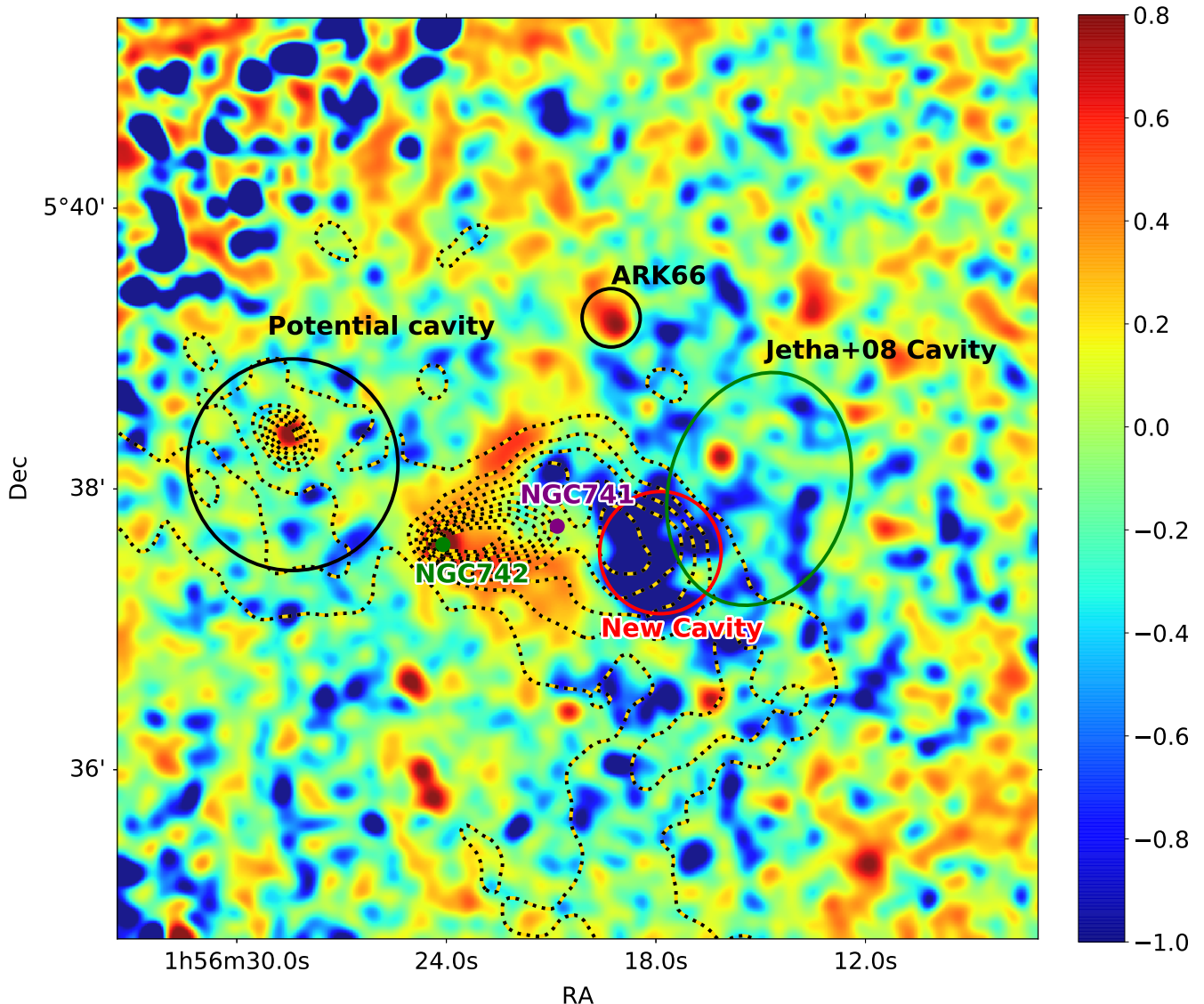


Figure 11. Residual image with respect to the double beta 2D model fit. The color scale shows the fractional residuals where positive values refer to an underestimated flux in the model. The dotted lines are the 3σ radio contours from 235 MHz GMRT observations. 1 arcmin = 21 kpc

not enough to explain the observed deficit. If we assume an ellipsoidal cavity elongated along the line of sight, a semi-major axis of 37 kpc is required, 4.6 times the size of the other axes.

The enthalpy and cavity power (based on the sound crossing timescale) of this newly detected spherical under-dense region is $4.9 \pm 0.5 \times 10^{57}$ erg and $5.1 \pm 0.5 \times 10^{42}$ erg s $^{-1}$, which would require 600 Myr to be consistent with the $4pV$ relation (Panagoulia et al. 2014b).

4.2.3. Potential east cavity

The interaction between NGC 742 and NGC 741 (see Section 4.3) might have affected the position of NGC 741. We take the central velocity dispersion measurements for both galaxies from Focardi & Malavasi (2012) and use the relations from McConnell et al. (2011) and Zahid et al. (2016) to get the stellar masses ($3.6 \times 10^{11} M_{\odot}$ for NGC 741, $5 \times 10^{10} M_{\odot}$ for NGC 742). Using this mass ratio of about 7 to 1, we conclude that

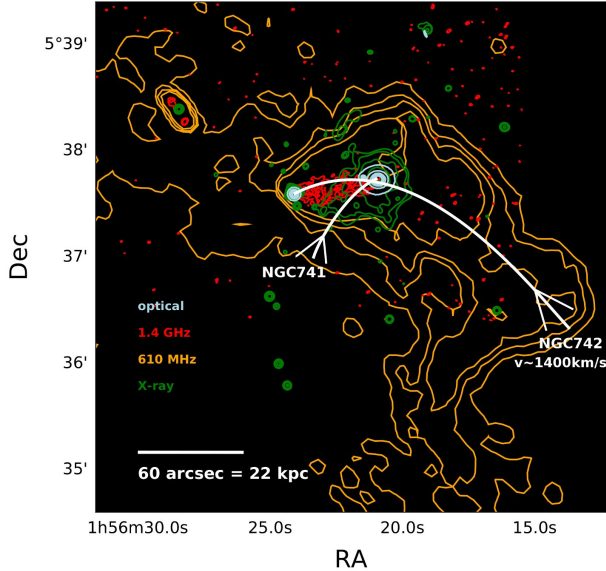


Figure 12. Illustration of the merging scenario of NGC 742 with the galaxy group.

a shift of NGC 741 of about 10 to 20 arcsec to the west (i.e., its current position) is plausible. Given the presence of the newly identified small western cavity, we might expect a second cavity on the eastern side of NGC 741, located further from the galaxy. The two cavities would have been roughly equidistant from NGC 741 before the encounter with NGC 742.

We do indeed see extended radio emission to the east of NGC 741, especially at 235 MHz and 610 MHz ("Potential cavity" in Fig. 11). This emission could be due to an old radio lobe inflated by NGC 741, although there is no emission at the same radius on the west side of NGC 741. Constructing a spectral index map from those two frequencies only (because of the high resolution), we find overall a rather steep index (> 2), with a few regions close to the flatter spectrum of NGC 742. It seems that part of the emission in this region might be powered by the AGN of NGC 742, with the remainder arising from an older outburst of NGC 741. We do not see indications at this position for an X-ray surface brightness decrease. This might have been obscured by the shock produced by NGC 742.

4.3. NGC 742 merging event

Our suggested scenario for the infall of NGC 742 into the NGC 741 group is summarized in Fig. 12. We conclude from the spectral index map of the south-west radio tail that NGC 742 approached the galaxy group with an approximate velocity of 1400 km s^{-1} . Its path is characterized by the remnant radio emission of the AGN, although the shape some of the more distant regions of the south-west tail might have been disturbed

by gas motions in the surrounding ICM. The surface brightness deficiency (classified as a smaller cavity in Section 4.2.2) might also be caused by the encounter of NGC 742 dragging gas away from this region. The fact that the deficit in counts in this region is larger than expected for an AGN inflated bubble, might point out that it is a superposition of multiple effects.

The close encounter with the BCG and the much denser ICM of NGC 741 caused the stripping of any gas associated with NGC 742 and may have also displaced some of the gas from the group core. The activity of the NGC 742 AGN may also have been enhanced, leading to the prominent head-tail structure. If one assumes that the shape of this head-tail source resembles a Mach cone, the velocity can be estimated from the cone-angle to be $\sim 1300 \text{ km s}^{-1}$, in good agreement with the velocity estimated from the spectral index map. The velocity of a head-tail radio source in a galaxy cluster can also be estimated from the radio jet curvature and cylindrical jet diameter (see e.g., Freeland & Wilcots 2011 or simulations by Morsony et al. 2013). We assume a jet velocity on the order of $0.1c$, and a ratio of jet curvature and cylindrical diameter of 3.75, and find a galaxy velocity of order 500 km s^{-1} , less than our other estimates. If we look at the optical recession velocities of NGC 741 and NGC 742 (Mahdavi & Geller 2004) we find a difference of 403 km s^{-1} . We assume this is the line-of-sight velocity component of NGC 742 relative to the galaxy group, while the projected velocity component is estimated from the trajectory (130 kpc) and the spectral aging 90 Myr to be 1410 km s^{-1} . This leads to a 3D velocity of 1466 km s^{-1} . This is in good agreement with the infall velocity due to the gravitational potential of the galaxy group if the infall of NGC 742 started at around R_{500} until the current position, 18 kpc away from the group center.

In the X-ray regime we reported several unexpected features for a cool core cluster or group: Perhaps the most notable is the X-ray bright filament between the core of NGC 741 and NGC 742, which consists of low entropy gas and is consistent with being stripped from NGC 742. Assuming a cylindrical shape, our spectral analysis of the X-ray data using an MCMC reveals that the filament is in rough pressure equilibrium with the surrounding medium ($4.3 \pm 0.9 \times 10^{-11} \text{ dyn cm}^{-2}$ in the filament and $3.4 \pm 0.2 \times 10^{-11} \text{ dyn cm}^{-2}$ in the surrounding). The filament could also be gas from the core of NGC 741, drawn outwards during the close encounter. The X-ray emission from the filament is slightly offset from the bent radio lobes of NGC 742 (see Fig. 12). The origin of the radio emission is attributed to the strongly bent jets of the AGN of NGC 742 and so it is plausible that it is not perfectly aligned with the X-ray emission. More evidence for a recent disruptive event in NGC 742 is provided by the rings visible in the optical image (Fig. 10).

In Figure 11 we see a V-shaped structure in the X-ray surface brightness residuals to the east of NGC 742. The position and shape of this feature might suggest that there is a cold or shock front present. We also see a temperature discontinuity in this region in Fig. 4. Taking spectra from the region of the increased surface brightness, and from the region to its east, shows that in the east, the temperature is about 75% higher, as would be expected for a cold front with a Mach number of about 1.7. Using the sound speed at this location, this Mach number implies a velocity for NGC 742 of $1100 \pm 66 \text{ km s}^{-1}$. This estimate is about 30% lower than the velocity from spectral aging, but given the many uncertainties in selecting the (pre-)shock region for the spectral extraction, and the assumptions in the radio spectral aging calculation, it still clearly confirms a supersonic motion.

4.4. Other merging activity

To the south-west of NGC 741 (~ 30 arcsec distance) we see a two arm-like features in the soft X-ray image. The first one, around 18 kpc length, is well aligned to the edge of the south-west radio-tail, while the other, approximately 16 kpc in length, is perpendicular to the first arm, pointing to the south. The origin of these features remains unclear, although they are likely related to the perturbation caused by the infalling galaxy NGC 742 (e.g., gas pushed aside during the encounter). In Fig. 1 (left) one can see that this X-ray filament is aligned with the radio emission tracing the infall of NGC 742.

We detect X-ray emission from other group member galaxies, including one with an X-ray tail. Although we do not see other head-tail radio sources, this clearly indicates further merging activity in this system. 35 arcsec, or 13 kpc, to the north-east of the core of NGC 741 we see a filament in the soft X-ray band. Extracting a spectrum of this region reveals that its temperature is consistent with the surrounding ICM. Although the abundance might be slightly higher (30%) in the region of the north-east filament, with the number of available counts we cannot be sure that this difference is statistically significant. Nevertheless, this region could be the remnant of an earlier merging interaction, i.e. ram pressure stripped gas. The sound-crossing time of the north-east filament is about 13 Myr.

5. SUMMARY AND CONCLUSIONS

We analyzed the kinematic and thermodynamic structure of the galaxy group NGC 741. This nearby group is caught in an unusual dynamical state and exhibits a recent merging event, with a member galaxy passing through the core region close to the BCG. Our results exploit data from recent long Chandra and XMM-Newton observations as well as from GMRT and VLA covering five frequencies between 150 MHz and 5 GHz. We also include constraints from the MWA GLEAM survey and

optical HST observations in drawing our conclusions, which can be summarized as follows:

- Our X-ray analysis shows that the group has a cool-core with a minimum temperature of about 0.5 keV. The peak temperature of the ICM, about 2 keV, is reached at 1.5 arcmin radius, and the total hydrostatic mass $M_{500} = 5.2 \pm 0.4 \times 10^{13} M_{\odot}$. The gas mass fraction is only about 3% at R_{2500} .
- We find several merging or infalling objects. Most prominent is NGC 742, only about 18 kpc in projection from the BCG. We detect three other X-ray bright galaxies, one of them with a tail indicative of gas stripping caused by its infall through the group. Residual gas filaments to the north-east of the BCG may indicate other past merger events.
- By developing a new algorithm based on the Iron-L line position (see also David et al. 2009) and the relative line flux, we are able to construct temperature and relative abundance maps even with limited numbers of counts. These maps show a hotter temperature to the east and cooler structure to the south of NGC 741. Along with the higher abundance in the center of the group, we see several peaks in the abundance map (confirmed using standard spectroscopic analysis), probably due to the stripped gas of merging galaxies, especially along the inferred path of NGC 742.
- The X-ray filament connecting NGC 742 and NGC 741 may itself be an X-ray tail, since its entropy is consistent with being gas stripped from NGC 742. High-resolution radio images also show a head-tail structure, slightly offset from the X-ray filament. We attribute the radio emission to the strongly bent jets of the AGN in NGC 742. The optical HST image reveals irregularities in the stellar component of the galaxy, which could be witnesses of the past interaction with the BCG.
- The large-scale radio emission shows a long (> 130 kpc) tail to the south-west of the BCG, which we interpret as older emission from the AGN of NGC 742. The radio spectral index map shows a clear steepening from a power-law index of -0.6 around NGC 742, to -1.3 and beyond at the end of the tail. We map the estimated spectral age along this tail and conclude that the time of last injection of energetic particles at the end of the tail was around 90 Myr ago.
- The ghost cavity to the west of the BCG cannot be confirmed. We discover a cavity at a closer distance, about 16 kpc from NGC 741. This region shows a much stronger surface brightness decrease and exhibits non-thermal radio emission.

The depth of the surface brightness deficit suggests that this cavity is very elongated (factor of 4.5) along the line of sight.

Given the large amount of multi-wavelength data available for this object, we are able to construct a detailed scenario for the history of the NGC 741 – NGC 742 interaction. Some uncertainties remain, particularly regarding the shape of the south-west radio tail, and the unexpected irregularity of the spectral steepening along its length. We conclude that the galaxy had a strong impact on the chemical composition of the galaxy group, and that since the interaction happened fairly recently, the creation of prominent gas-sloshing features can be expected in the future as the group core responds to the impetus imparted by the interaction.

ACKNOWLEDGEMENTS

The authors acknowledge the comments provided by the anonymous referee, which helped to improve this

paper. The authors would like to thank Mark Birkinshaw, Diana Worrall, Reinout van Weeren and Tracy Clarke for helpful discussions. Support for this work was provided by the National Aeronautics and Space Administration (NASA) through Chandra Award Number GO3–14143X and GO5–16135X issued by the Chandra X-ray Observatory Center (CXC), which is operated by the Smithsonian Astrophysical Observatory (SAO) for and on behalf of NASA under contract NAS8–03060. Basic research in radio astronomy at the Naval Research Laboratory is supported by 6.1 base funding. MJH and SD are funded by a Marsden Fund Grant (PI Johnston-Hollitt) administered by the Royal Society of New Zealand. This research made use of Astropy, a community-developed core Python package for Astronomy.

REFERENCES

- Allen, S. W. 1995, *MNRAS*, 276, 947
- Asplund, M., Grevesse, N., Sauval, A. J., & Scott, P. 2009, *ARA&A*, 47, 481
- Baars, J. W. M., Genzel, R., Pauliny-Toth, I. I. K., & Witzel, A. 1977, *A&A*, 61, 99
- Becker, R. H., White, R. L., & Edwards, A. L. 1991, *ApJS*, 75, 1
- Bharadwaj, V., Reiprich, T. H., Schellenberger, G., et al. 2014, *A&A*, 572, A46
- Bhattacharya, S., Habib, S., Heitmann, K., & Vikhlinin, A. 2013, *ApJ*, 766, 32
- Birkinshaw, M., & Davies, R. L. 1985, *ApJ*, 291, 32
- Birzan, L., Rafferty, D. A., McNamara, B. R., Wise, M. W., & Nulsen, P. E. J. 2004, *ApJ*, 607, 800
- Briggs, D. S. 1995, PhD thesis, New Mexico Institute of Mining Technology, Socorro, New Mexico, USA
- Buote, D. A. 2000, *MNRAS*, 311, 176
- Carilli, C. L., Perley, R. A., Dreher, J. W., & Leahy, J. P. 1991, *ApJ*, 383, 554
- Cash, W. 1979, *ApJ*, 228, 939
- Cavagnolo, K. W., Donahue, M., Voit, G. M., & Sun, M. 2009, *ApJS*, 182, 12
- Condon, J. J., Cotton, W. D., Greisen, E. W., et al. 1998, *AJ*, 115, 1693
- David, L. P., Jones, C., Forman, W., et al. 2009, *ApJ*, 705, 624
- Eckmiller, H. J., Hudson, D. S., & Reiprich, T. H. 2011, *A&A*, 535, A105
- Eilek, J. A., Burns, J. O., O’Dea, C. P., & Owen, F. N. 1984, *ApJ*, 278, 37
- Eke, V. R., Navarro, J. F., & Frenk, C. S. 1998, *ApJ*, 503, 569
- Focardi, P., & Malavasi, N. 2012, *ApJ*, 756, 117
- Foster, A. R., Ji, L., Smith, R. K., & Brickhouse, N. S. 2012, *ApJ*, 756, 128
- Freeland, E., & Wilcots, E. 2011, *ApJ*, 738, 145
- George, K. 2017, *A&A*, 598, A45
- Giacintucci, S., O’Sullivan, E., Vrtilik, J., et al. 2011, *ApJ*, 732, 95
- Hogan, M. T., McNamara, B. R., Pulido, F., et al. 2017, *ApJ*, 837, 51
- Huchra, J. P., Vogeley, M. S., & Geller, M. J. 1999, *ApJS*, 121, 287
- Intema, H. T., Jagannathan, P., Mooley, K. P., & Frail, D. A. 2017, *A&A*, 598, A78
- Jarrett, T. H., Masci, F., Tsai, C. W., et al. 2013, *AJ*, 145, 6
- Jeltema, T. E., Binder, B., & Mulchaey, J. S. 2008, *ApJ*, 679, 1162
- Jetha, N. N., Hardcastle, M. J., Babul, A., et al. 2008, *MNRAS*, 384, 1344
- Konstantopoulos, I. S., Gallagher, S. C., Fedotov, K., et al. 2010, *ApJ*, 723, 197
- Lane, W. M., Cotton, W. D., van Velzen, S., et al. 2014, *MNRAS*, 440, 327
- Lavaux, G., & Hudson, M. J. 2011, *MNRAS*, 416, 2840
- Lee, J. C., Hwang, H. S., & Ko, J. 2013, *ApJ*, 774, 62
- Lovisari, L., Reiprich, T. H., & Schellenberger, G. 2015, *A&A*, 573, A118
- Mahdavi, A., & Geller, M. J. 2004, *ApJ*, 607, 202
- Mapelli, M., & Mayer, L. 2012, *MNRAS*, 420, 1158

- McConnell, N. J., Ma, C.-P., Gebhardt, K., et al. 2011, *Nature*, 480, 215
- McDonald, M., Stalder, B., Bayliss, M., et al. 2016, *ApJ*, 817, 86
- Mernier, F., de Plaa, J., Lovisari, L., et al. 2015, *A&A*, 575, A37
- Morsony, B. J., Miller, J. J., Heinz, S., et al. 2013, *MNRAS*, 431, 781
- Nair, P. B., & Abraham, R. G. 2010, *ApJS*, 186, 427
- Panagoulia, E. K., Fabian, A. C., & Sanders, J. S. 2014a, *MNRAS*, 438, 2341
- Panagoulia, E. K., Fabian, A. C., Sanders, J. S., & Hlavacek-Larrondo, J. 2014b, *MNRAS*, 444, 1236
- Perley, R. A., & Butler, B. J. 2017, *ApJS*, 230, 7
- Ponman, T. J., Cannon, D. B., & Navarro, J. F. 1999, *Nature*, 397, 135
- Rafferty, D. A., McNamara, B. R., & Nulsen, P. E. J. 2008, *ApJ*, 687, 899
- Sanderson, A. J. R., Ponman, T. J., & O'Sullivan, E. 2006, *MNRAS*, 372, 1496
- Scaife, A. M. M., & Heald, G. H. 2012, *MNRAS*, 423, L30
- Schellenberger, G., & Reiprich, T. H. 2015, *A&A*, 583, L2
- . 2017, *MNRAS*, 469, 3738
- Slee, O. B., Roy, A. L., Murgia, M., Andernach, H., & Ehle, M. 2001, *AJ*, 122, 1172
- Sun, M., Forman, W., Vikhlinin, A., et al. 2003, *ApJ*, 598, 250
- Sun, M., Jones, C., Forman, W., et al. 2006, *ApJL*, 637, L81
- Sun, M., Voit, G. M., Donahue, M., et al. 2009, *ApJ*, 693, 1142
- Tozzi, P., & Norman, C. 2001, *ApJ*, 546, 63
- Voit, G. M., Donahue, M., Bryan, G. L., & McDonald, M. 2015, *Nature*, 519, 203
- Wayth, R. B., Lenc, E., Bell, M. E., et al. 2015, *PASA*, 32, e025
- Whiting, M. T. 2012, *MNRAS*, 421, 3242
- Willingale, R., Starling, R. L. C., Beardmore, A. P., Tanvir, N. R., & O'Brien, P. T. 2013, *MNRAS*, 431, 394
- Zahid, H. J., Geller, M. J., Fabricant, D. G., & Hwang, H. S. 2016, *ApJ*, 832, 203
- ZuHone, J. A., Markevitch, M., & Johnson, R. E. 2010, *ApJ*, 717, 908

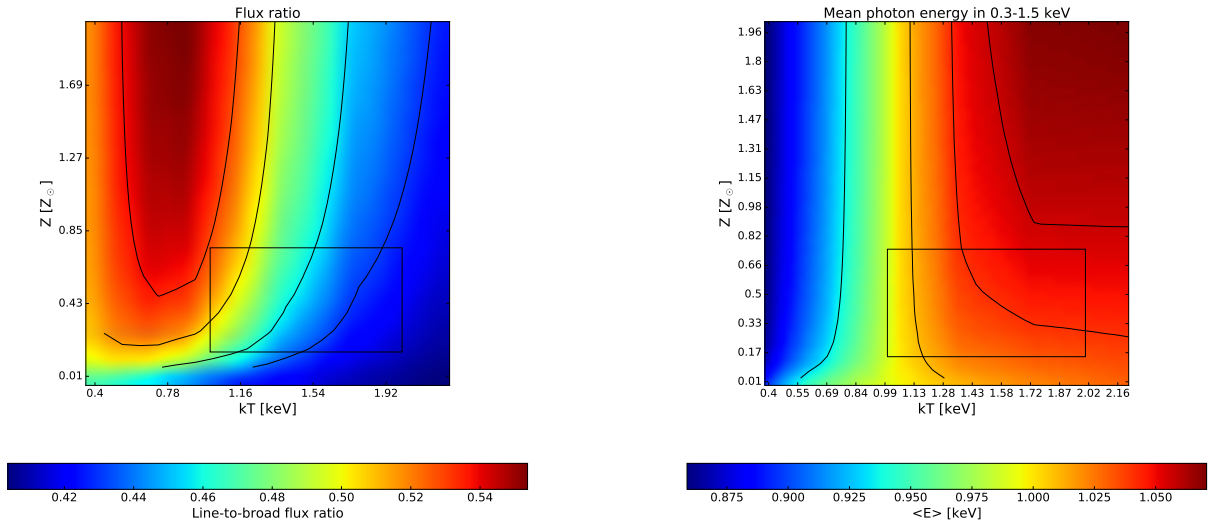


Figure 13. Simulations to connect the two observables with ICM temperature and metallicity. Both images show one slice of the 3D cubes (for the maximum source-to-background ratio). The black box shows an important range of the two parameters.

APPENDIX

A. TEMPERATURE AND ABUNDANCE MAPS

Spatial variations of temperature and abundances of heavy elements in the ICM are crucial to investigate the merging history of a galaxy cluster. Apart from radial profiles the information provided by detailed maps is of great importance because merging processes usually create an asymmetric distribution of the temperature and abundances. The ability to constrain with reasonable accuracy the temperature and abundance from a spectral fit depends strongly on the number of counts, but also on the temperature of the system. For low temperature galaxy groups one needs several hundreds of counts to constrain the temperature and even more for a reliable abundance measurement. With available exposure times, this does not allow the detailed investigation of NGC741 by a temperature or abundance map, especially not in lower surface brightness regions.

We present a method to create temperature and abundance maps for low temperature galaxy groups (up to 2 keV) by combining the information from images of the system in three different bands: It has already been shown (David et al. 2009) that the mean energy of photons in a soft band covering the Fe-L line complex is a good measure for the ICM temperature and fairly independent of the abundance of heavy elements. The flux of the Fe-L line itself strongly depends on the abundance. By measuring the flux of the Fe-L line with respect to a broad band flux an observable for the abundance can be constructed. This observable still depends on the gas temperature, but this influence can be almost completely eliminated by combining the new observable with the mean energy.

Our simulations show that there exists a clear, almost abundance independent, relation between the mean photon energy and the ICM temperature. Furthermore, the ratio of the Fe-L line flux to broad band flux is sensitive to the abundance. But the two observables, the line-to-broad-band flux ratio and the mean photon energy have both dependencies on the ICM temperature and abundance, and also they depend on the source to background ratio.

We simulate spectra with an absorbed `apec` model (redshift and N_{H} frozen to cluster values) and give 20 uniformly distributed temperatures, (0.4–2.2) keV, 20 different abundances, (0.01–2.0) Z_{\odot} , and 10 different source to background ratios, 0.5 – 140, to construct a 3D matrix for each observable. These matrices are linearly interpolated to obtain the most likely values of temperature and abundance at each pixel of the input image. Figure 13 shows the one slice of the 3D matrices at maximum source-to-background ratio.

For the simulations we use the same responses created for the actual observations to account for the low energy degrading of the Chandra effective area. For the combination of more than one observation we weight them in the simulations according to their actual exposure times.

The actual images are produced in the the (0.3 – 4) keV band for the broad flux, the (0.7 – 1.3) keV band for the Fe-L line flux, and the (0.3 – 1.5) keV band for the mean energy to estimate the gas temperature. For our purposes these bands turned out to be well suited. Especially the band to determine the mean photon energy has to be extended toward higher energies to also allow a temperature determination up to 2 keV. To have comparable statistics in each spatial bin, we create a mask using the adaptive binning task `dmnautilus` and we require a signal-to-noise of at least 10 in the the Fe-L line band. Point sources are detected via the ciao task `wavdetect` and excluded for the analysis. It turns out that strong unremoved point sources like AGNs show up in the abundance map as regions with very low abundance.

We tested our results for the influence of multi temperature components. As suggested in [Buote \(2000\)](#), the Iron bias effect produces low-biased abundance measurements in multi temperature spectra which are fitted with just a single component. We estimated if this effect is also present in our method to produce an abundance map. We find that in general the maps are affected by the Iron bias in a very similar way as the spectral fit of a single temperature component. For example, for 0.4 keV and 1 keV gas with a emission measure ratio (cold-to-hot, EMR) of 1, we find a 60% lower abundance for both methods. If we change the EMR to 0.1 (more hotter gas), we find a lower abundance of 12% for the spectral fit, and 20% for the map. Instead if we have 10 times more colder gas than hotter, we find 44% lower abundances for the map and 52% for the spectral fit. If we increase the temperature of the cold component, we also find that the difference of the map abundance to the real one is smaller. In high quality data an indication for multi phase gas is a bad spectral fit, e.g., $\chi^2 \gg 1$. Since we have no measure of the goodness of fit for a thermal model available in our temperature and abundance maps, we cannot use this quantity to alleviate the influence of the iron bias.